BEILSTEIN JOURNAL OF ORGANIC CHEMISTRY

Interfragment interactions in outer-sphere radical addition control *Z*-selectivity in iron-catalyzed allene dialkylation

Zihan Li, Yin-Hon Yeung and Xinglong Zhang*

Full Research Paper

Open Access

Address:
Department of Chemistry, The Chinese University of Hong Kong, Shatin, New Territories, Hong Kong 999077, Special Administration Region of the People's Republic of China

Email:
Xinglong Zhang* - xinglong.zhang@cuhk.edu.hk

* Corresponding author

Keywords:
allene difunctionalization; density functional theory; iron catalysis; radical mechanism; *Z*-selectivity

Beilstein J. Org. Chem. **2026,** *22,* 1761–1772.
https://doi.org/10.3762/bjoc.22.142

Received: 25 July 2026
Accepted: 10 November 2026
Published: 24 November 2026

This article is part of the thematic issue "Young investigators in earth-abundant metal catalysis".

Guest Editor: G. Lefevre

© 2026 Li et al.; licensee Beilstein-Institut.
License and terms: see end of document.

Abstract

The stereoselective radical difunctionalization of allenes offers an efficient route to highly substituted alkenes, but controlling the geometry of the retained C=C-bond remains challenging because of the complex open-shell mechanisms involved. Recently, an iron-catalyzed three-component dialkylation was reported to provide light-free access to acyclic, all-carbon trisubstituted *Z*-alkenes through a kinetically controlled radical process. Beyond addressing a longstanding synthetic challenge, this transformation provides a valuable platform for examining how iron-mediated open-shell reactivity governs radical addition and stereochemical control. Our results support outer-sphere ethyl-radical addition to an iron-bound allene as both the rate- and stereo-determining step. The preference for the *Z*-forming pathway arises from more favorable interactions in the corresponding transition state, whereas the subsequent radical–radical C–C reductive coupling proceeds with a substantially lower barrier. Additional substituent comparisons show that the balance between distortion and interfragment interaction depends on the structures of the allene and the attacking radical. Together, these analyses extend the existing mechanistic understanding by providing a quantitative account of the energetic factors underlying stereoselectivity and their responses to changes in substrate structures. Effects of ligands in stereoinduction were unraveled by comparing the ferrocene ligand with high *Z*-selectivity, to a flat, tridentate terpyridine *N,N,N*-pincer ligand. Alternative radical-addition pathways were also investigated to assess competition with the productive pathway and possible reactivities to give side-products.

Introduction

Allenes are valuable synthons in modern organic synthesis because their cumulated diene structure gives rise to reactivity patterns distinct from those of conventional alkenes and alkynes [1,2]. Their orthogonal π-system enables selective bond formation at different positions of the three-carbon framework, making allenes versatile precursors for the construction of struc-

turally diverse products [3-6]. Among the diverse transformations of allenes, radical functionalization has emerged as an efficient strategy for generating molecular complexity [7-9]. In particular, radical 1,2-difunctionalization enables the installation of two substituents at adjacent carbon atoms while preserving one C=C bond, thereby providing direct access to highly functionalized alkenes [10]. Representative reactions illustrate the mechanistic diversity of this strategy (Scheme 1A): Wu and co-workers [11] developed a visible-light-promoted oxyalkenylation of phosphinylallenes, in which a photochemically gener-

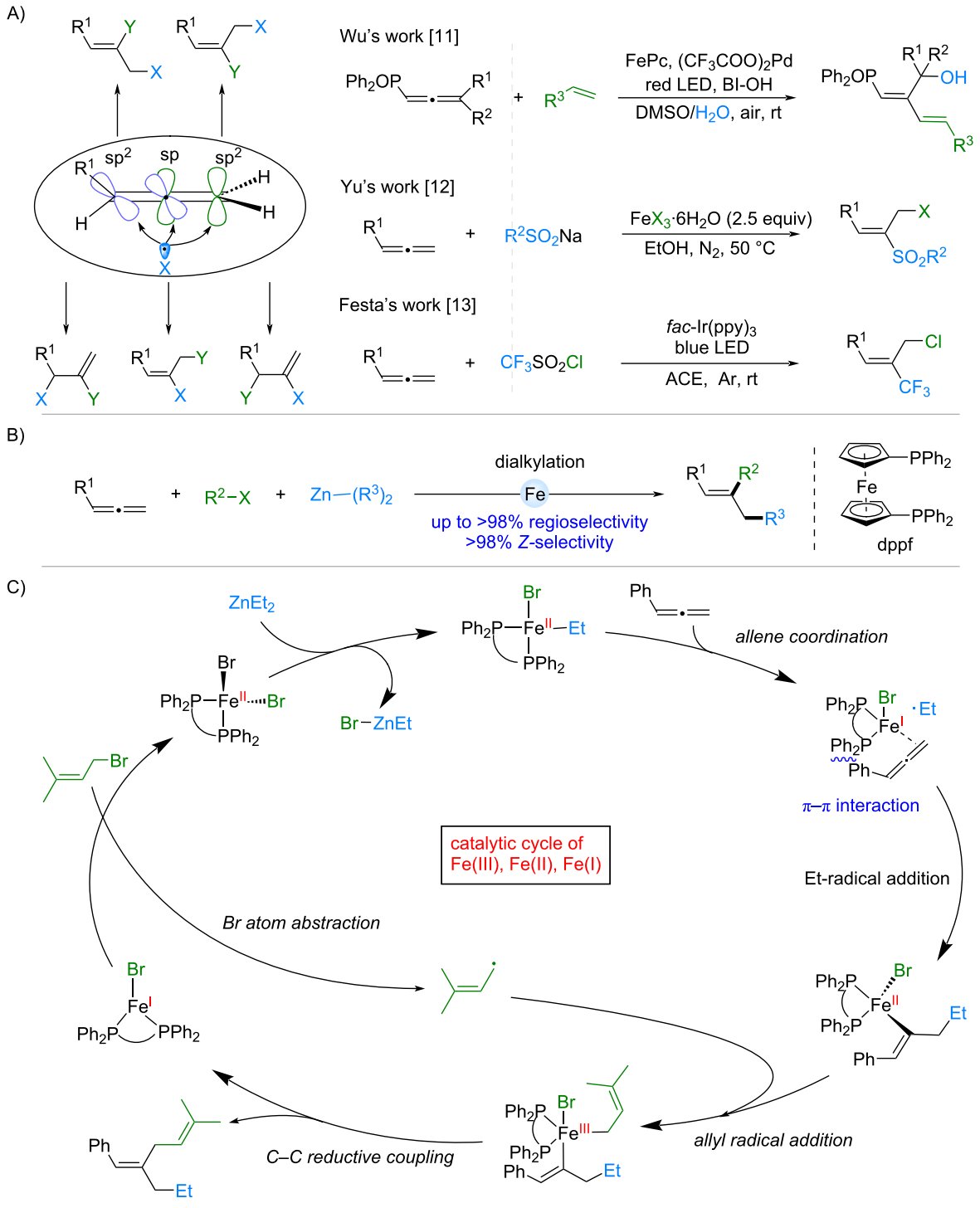

Scheme 1: A) Representative radical 1,2-difunctionalizations of allenes. B) Iron-catalyzed dialkylation for *Z*-alkene synthesis. C) Proposed catalytic cycle.

ated hydroxyl radical adds to a terminal allene carbon. In a complementary approach, Yu and co-worker [12] reported an Fe(III)-mediated chlorosulfonylation in which sulfonyl radicals generated from sodium sulfinates add to the central carbon of the allene, followed by oxidation to an allylic carbocation and terminal chlorination. More recently, Festa, Voskressensky, and co-workers [13] disclosed a photoredox chlorotrifluoromethylation of allenes, in which trifluoromethyl radicals add to the terminal carbon of the allene before oxidation to allylic carbocations and chloride trapping. Collectively, these studies demonstrate that radical allene 1,2-difunctionalization can involve different sites of radical addition, open-shell intermediates, and termination pathways. Such mechanistic diversity can strongly influence both regio- and stereochemical outcomes [10], highlighting the value of detailed mechanistic analysis for understanding selectivity in radical allene-to-alkene transformations.

The selective formation of *Z*-alkenes represents an important stereochemical objective in allene-to-alkene transformations. *Z*-Alkenes are valuable synthetic motifs and versatile intermediates for stereospecific downstream transformations [14], yet they are generally less thermodynamically stable than the corresponding *E*-isomers, making their selective formation and preservation challenging [15-17]. Against this background, Koh and co-workers [18] reported an iron-catalyzed three-component dialkylation of allenes that couples substituted allenes with alkyl electrophiles and organozinc reagents to provide kinetically controlled access to acyclic, all-carbon trisubstituted *Z*-alkenes, which remain challenging targets in stereoselective alkene synthesis (Scheme 1B). The use of iron as the catalyst is particularly noteworthy, given its natural abundance, low cost, and ability to access multiple oxidation and spin states that support single-electron reactivity [19,20]. Notably, the radical transformation proceeds under light-free conditions [18]. Beyond its synthetic value, this strategy for *Z*-alkene synthesis provides a useful mechanistic framework for examining how iron-mediated single-electron steps control radical reactivity and give rise to kinetic *Z*-selectivity.

Previous computational studies have explored radical addition to metal-associated π-systems and competing C–C-bond-forming pathways, providing insights into how coordination environments and noncovalent interactions influence reactivity and selectivity [21-24]. These studies motivate a closer examination of outer-sphere radical addition and its role in stereochemical control in iron-catalyzed allene dialkylation. Density functional theory (DFT) calculations supporting the proposed mechanism were previously reported by Zhang, Koh and co-workers [18]. Building on this established mechanistic framework, these calculations are reexamined and supplemented with additional analyses of competing pathways and the molecular origin of the *Z*/*E*-stereoselectivity. In particular, the thermochemical treatment is refined by supplementing the previously applied quasi-RRHO (rigid-rotor harmonic oscillator) correction [25] of vibrational entropies with the Head-Gordon quasi-RRHO correction [26], to provide a more refined description of the relative Gibbs energies along the catalytic pathway. Second, given the sensitivity of open-shell iron spin-state energetics to the choice of exchange-correlation functional [27], all stationary points are reassessed by single-point calculations on the previously B3LYP [28] -D3BJ [29] -optimized geometries, using the global-hybrid meta-NGA MN15 functional [30], which is benchmarked to perform well in describing multireference systems, thus providing an independent functional-level assessment [27,31]. Third, based on the proposed catalytic cycle shown in Scheme 1C, the individual computational results are integrated to provide a unified mechanistic description, with particular attention to the molecular origin of the *Z*/*E*-selectivity. Distortion/interaction analysis, independent computational variation of the allene substituent and the attacking radical, and examination of alternative radical-addition pathways are further used to quantify the factors governing stereoselectivity and assess competing C–C-bond-forming processes.

Results and Discussion

The overall Gibbs energy profile of the iron-catalyzed three-component allene dialkylation using separately B3LYP-D3BJ/def2-TZVP and MN15/def2-TZVP single-point energy corrections with implicit tetrahydrofuran (THF) solvent correction on the Gibbs energies obtained at B3LYP-D3BJ/def2-SVP level of theory is shown in Figure 1. The catalytic sequence involves two mechanistically distinct C–C-bond-forming events: an outer-sphere radical addition to the iron-bound allene, followed by coupling of the resulting alkenyliron intermediate with a second carbon-centered radical. The catalytic cycle begins with the bisphosphine-ligated Fe(II) alkyl bromide complex **I**, which is formed from the Fe(III) precatalyst and $ZnEt_2$, through a strongly exergonic reduction–transmetalation reaction (the calculated Gibbs energy change ΔG_r = −51.2 (−55.8) kcal/mol, Supporting Information File 1, section III). Among the spin states examined, the quintet state of **I** was adopted as the zero-energy reference, whereas the corresponding triplet and singlet states are higher in energy. Although the MN15 single-point correction substantially reduces the triplet–quintet energy gap from 11.7 to 3.0 kcal/mol, the quintet state remains the ground state for both functionals. The singlet state remains considerably less favorable under both computational treatments. Coordination of the allene to **I** is accompanied by the release of an ethyl radical, which adds to the less hindered terminal carbon through the outer-sphere transition state **TS1** with an activation barrier of 26.4 (25.1) kcal/mol, affording the *Z*-alkenyliron intermediate **IV** at −21.5 (−23.1) kcal/mol. The competing tran-

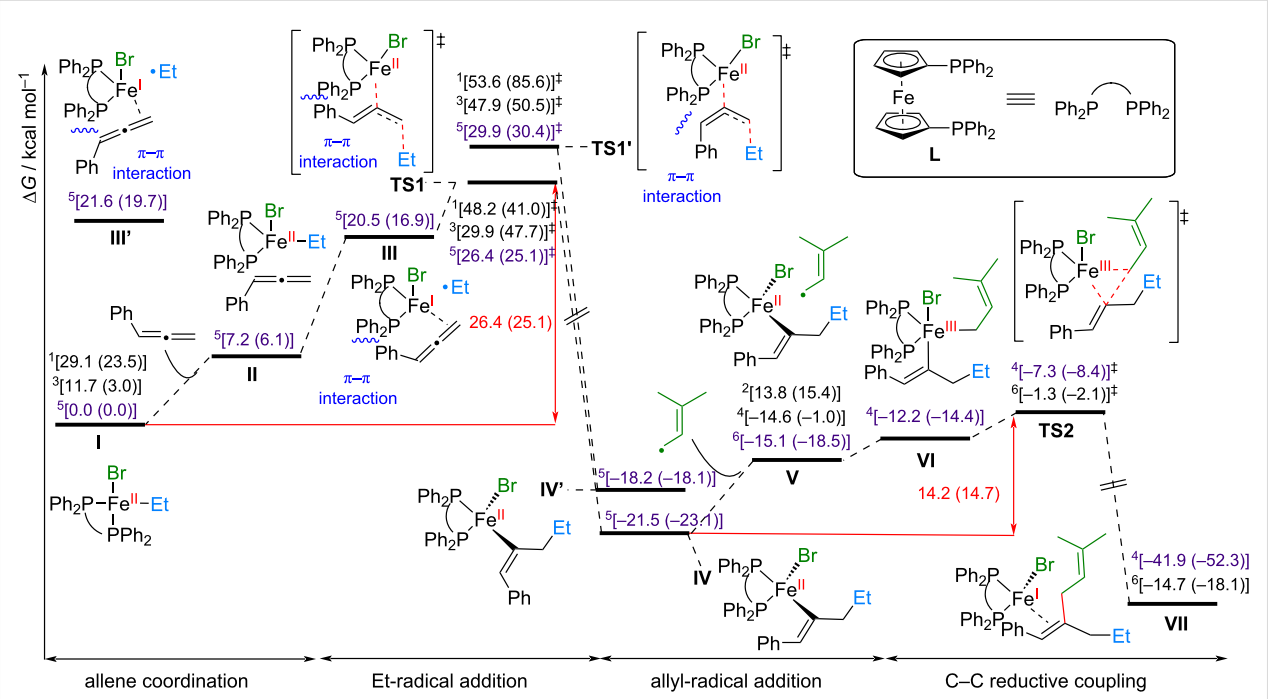

Figure 1: Computed Gibbs free energy profile for iron-catalyzed allene dialkylation. Values in square brackets are obtained at the SMD (THF)-B3LYP-D3BJ/def2-TZVP//B3LYP-D3BJ/def2-SVP level of theory and values in parentheses are obtained at the SMD (THF)-MN15/def2-TZVP//B3LYP-D3BJ/def2-SVP level of theory. Superscripts in front of square brackets denote the spin states of the species.

sition state **TS1′**, which leads to the corresponding *E*-alkenyl-iron intermediate **IV′**, has a higher barrier of 29.9 (30.4) kcal/mol; **IV′** is likewise 3.3 (5.0) kcal/mol higher in energy than **IV**. For this key step, the possible spin states of both competing transition states were also examined. For **TS1**, using SMD (THF)-B3LYP-D3BJ/def2-TZVP//B3LYP-D3BJ/def2-SVP results, the quintet state is the lowest in energy at 26.4 kcal/mol, whereas the triplet and open-shell singlet states lie at 29.9 and 48.2 kcal/mol, respectively. Similarly, **TS1′** is most favorable on the quintet state, with an activation barrier of 29.9 kcal/mol, while the corresponding triplet and open-shell singlet transition states are substantially higher in energy at 47.9 and 53.6 kcal/mol, respectively. The SMD (THF)-MN15/def2-TZVP single-point treatment preserves this preference, giving quintet barriers of 25.1 and 30.4 kcal/mol for **TS1** and **TS1′**, respectively. These results indicate that both competing radical-addition pathways preferentially proceed on the quintet state.

Following formation of **IV**, association of the allylic radical gives intermediate **V**. Under the B3LYP-D3BJ energy treatment, the quartet and sextet states of **V** are nearly degenerate at −14.6 and −15.1 kcal/mol, respectively, whereas the doublet state is much less favorable at 13.8 kcal/mol. MN15 single-point calculations likewise favor the higher-spin states, with the sextet becoming the lowest-energy state. From **V**, reductive C(sp^2)–C(sp^3) coupling proceeds through **TS2** with an activation barrier of 14.2 (14.7) kcal/mol to afford the *Z*-dialkylated alkene product. The final product-release step is accompanied by regeneration of the catalytically active species **I** and generation of the allylic radical. This process is also thermodynamically favorable (ΔG_r = −17.5 (−10.7) kcal/mol; Supporting Information File 1, section III). The thermodynamic stabilities of the *E*- and *Z*-alkene products were also compared. The two isomers are nearly isoenergetic, with the *E*-isomer being only 0.2 (0.04) kcal/mol more stable than the *Z*-isomer. This negligible thermodynamic preference cannot account for the experimentally observed predominance of the *Z*-product, confirming that the stereochemical outcome is under kinetic rather than thermodynamic control.

The computed profile therefore identifies the initial radical addition to the coordinated allene as both the rate- and stereo-determining event. Because formation of **IV** is effectively irreversible relative to the subsequent radical coupling step (the barrier from **IV**/**IV′** back to **III** via **TS1**/**TS1′** is much higher than the barrier from **IV**/**IV′** to **VII** via **TS2**), the energy difference between **TS1** and **TS1′** is directly translated into the observed kinetic preference for the *Z*-alkene.

To identify the pathway responsible for the stereo-determining C–C-bond-forming step, two mechanistically distinct pathways were examined: outer-sphere ethyl-radical addition and inner-

sphere migratory insertion. In the outer-sphere pathway, an ethyl radical that is not coordinated to the iron center directly attacks the iron-coordinated allene. In the inner-sphere pathway, by contrast, the coordinated allene undergoes migratory insertion into the Fe–Et bond in **II**. The optimized transition-state structures and corresponding activation barriers are shown in Figure 2. For the outer-sphere pathway, **TS1** and **TS1′** have activation barriers of 26.4 and 29.9 kcal/mol, respectively, whereas the corresponding inner-sphere transition states **TS1a** and **TS1a′** require substantially higher barriers of 40.9 and 39.3 kcal/mol. The MN15 single-point calculations give the same mechanistic preference, with barriers of 25.1 and 30.4 kcal/mol for **TS1** and **TS1′**, respectively, compared with 38.3 and 35.9 kcal/mol for **TS1a** and **TS1a′**. Notably, **TS1a′** is lower in energy than **TS1a** under both computational treatments, predicting a *Z*/*E*-preference opposite to that observed experimentally if the inner-sphere mechanism were operative. These results show that the inner-sphere migratory insertion is kinetically disfavored relative to the outer-sphere ethyl-radical addition. Inspection of the DFT-optimized structures (Supporting Information File 1, Figure S3) suggests that the higher barriers of the inner-sphere pathways may arise from the steric congestion and greater geometric reorganization required to bring the Fe–Et bond and the coordinated allene into a suitable insertion geometry; a requirement that does not apply to outer-sphere radical addition.

We further examined two additional reactivity pathways: 1) allylic radical addition to the iron-coordinated allene, as compared to ethyl-radical addition and 2) ethyl-radical addition to free allene. As shown in Figure 3A, the quintet transition state **TS1_allylic** is 15.3 (18.3) kcal/mol higher in free energy than **TS1**, supporting the ethyl-radical addition as the preferred first C–C-bond-forming step.

We next considered the reaction of the ethyl radical with an additional molecule of free phenylallene, leaving the Fe–allene complex as a spectator (Figure 3B). The corresponding encounter complex **INT1** and transition state **TS1_Fe_free** lie at 21.1 (17.9) and 30.8 (30.2) kcal/mol, respectively (the **^{4}Fe_I_complex** was used in this pathway because the **^{2}Fe_I_complex** is 26.0 (29.6) kcal/mol higher in energy). Because the Fe-free pathway consumes one additional molecule of free allene relative to the pathway through **TS1**, the concentration-dependent free-energy difference between **TS1** and **TS1_Fe_free** can be estimated as: $\Delta\Delta G^{\ddagger}_{\mathrm{eff}}$ (**TS1_Fe_free** − **TS1**) = $\Delta\Delta G^{\ddagger,\circ}$ − $RT\ln([\text{allene}]/1.0\ \text{M})$, where $\Delta\Delta G^{\ddagger,\circ}$ = 4.4 (5.1) kcal/mol. Under the ideal-solution approximation, even at an assumed allene concentration of 10.0 M, **TS1_Fe_free** remains $\Delta\Delta G^{\ddagger}_{\mathrm{eff}}$ = 2.9 (3.6) kcal/mol less favorable than **TS1** at 333.15 K, indicating that the Fe-free pathway remains kinetically disfavored relative to the pathway through **TS1**.

Because the origin of the *Z*/*E*-selectivity is central to this transformation, the competing transition states **TS1** and **TS1′** were analyzed using distortion/interaction (D/I) [32,33], spin-density and noncovalent interaction (NCI) analyses (Figure 4A). In the distortion/interaction analysis, the system is divided into an

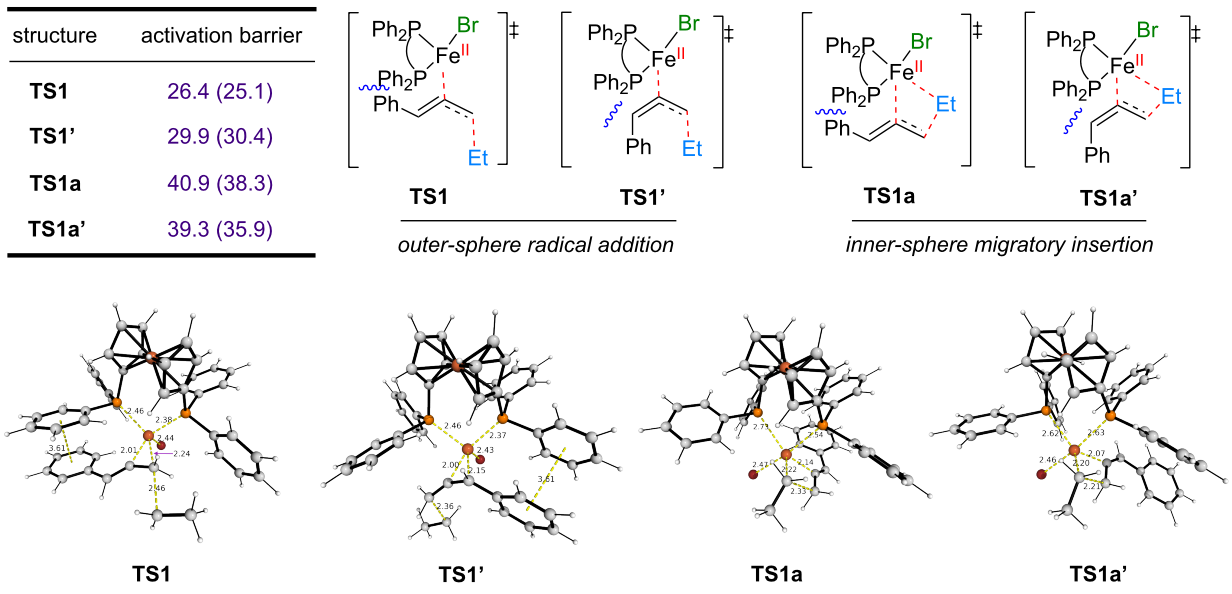

Figure 2: DFT-optimized structures and activation barriers for (a) outer-sphere ethyl-radical addition and (b) inner-sphere migratory insertion. Activation barriers are given in kcal/mol, with B3LYP-D3BJ values shown with MN15 values in parentheses.

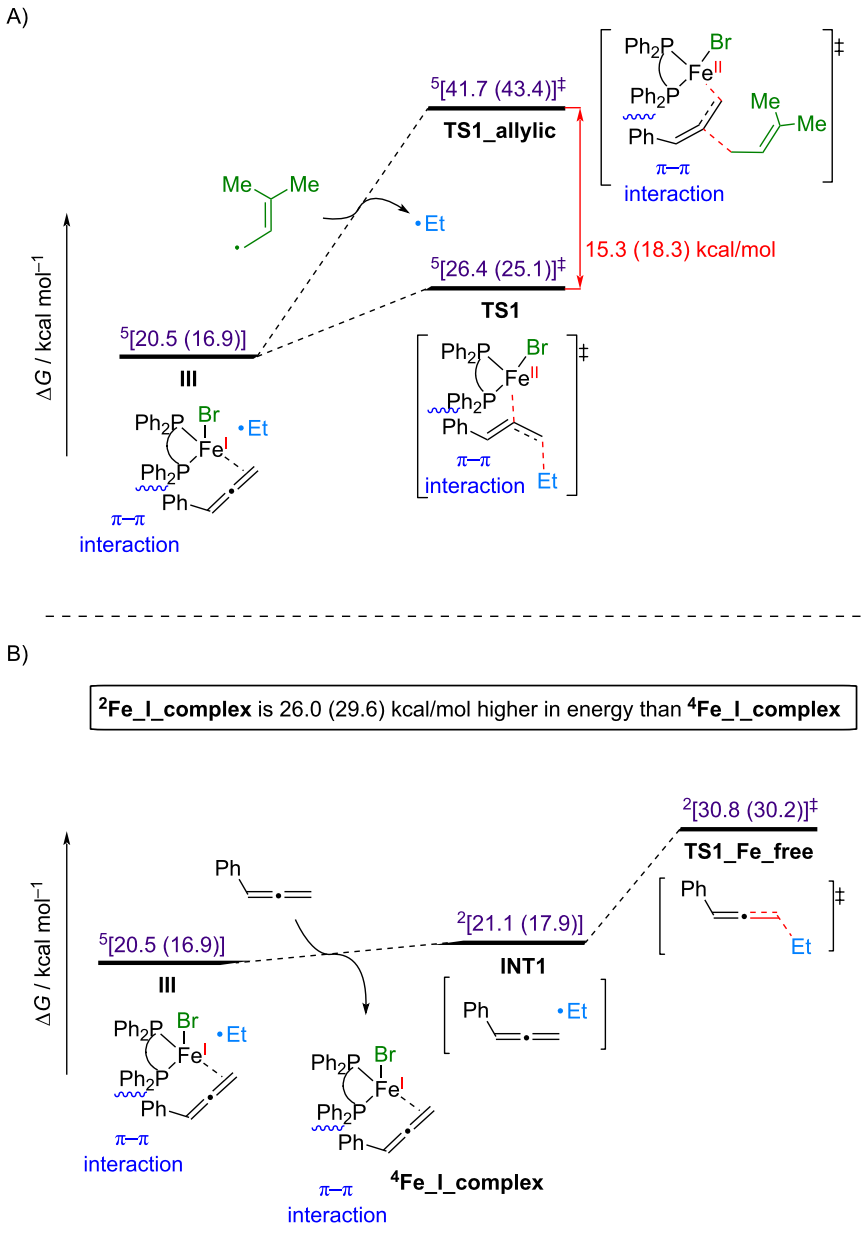

Figure 3: Two additional reactivity pathways: A) allylic radical addition to the iron-coordinated allene; B) ethyl-radical addition to free phenylallene, **^{4}Fe_I_complex** is retained as a spectator in the energy accounting. Relative Gibbs free energies are referenced to **I_quintet** and given in kcal/mol, with MN15 single-point values in parentheses.

Fe–ligand–allene fragment and an ethyl-radical fragment. For the D/I analysis, energy differences are defined as the unprimed minus the primed transition-state values; negative values therefore favor the major-product-forming transition state. At the B3LYP-D3BJ level, the Fe–ligand–allene fragment in **TS1** incurs a distortion penalty 1.2 kcal/mol greater than that in **TS1′**. This unfavorable distortion is more than compensated by an interaction energy that is 2.9 kcal/mol more favorable between the ethyl radical and the distorted Fe–ligand–allene fragment, resulting in an overall electronic-energy preference of 1.9 kcal/mol for **TS1**. The MN15 calculations provide the same interpretation, with an overall energy preference of 2.5 kcal/mol for **TS1**. Thus, the kinetic preference for the *Z*-forming pathway arises primarily from the more favorable interfragment interaction established during ethyl-radical addition, rather than from a lower distortion penalty. Spin-density analysis reveals broadly similar open-shell electronic structures for **TS1** and **TS1′**, with substantial spin density located on both the iron center and the approaching ethyl fragment, consistent with a common outer-sphere radical-addition mechanism. NCI analy-

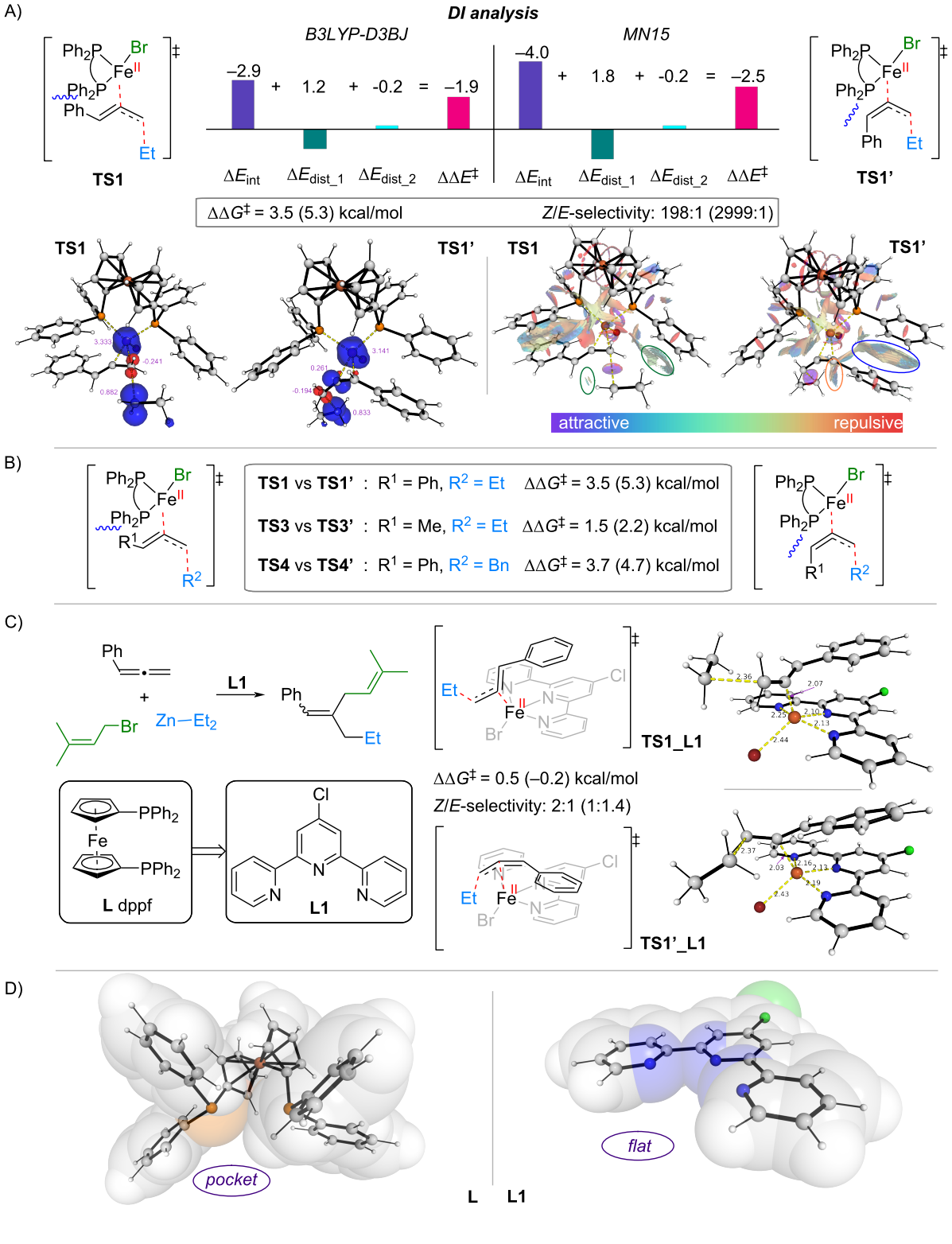

Figure 4: A) Distortion/interaction, spin-density (isosurface value = 0.01 a.u.), and NCI analyses of **TS1** and **TS1'**. B) Effects of the allene substituent (R^1) and the attacking radical (R^2) on the calculated free-energy differences between the competing transition states. Positive $\Delta\Delta G^‡$ values indicate a preference for the *Z*-forming transition state. C) Competing *Z*- and *E*-forming transition states with ligand **L1**. D) Structures and van der Waals surface representations of ligands **L** and **L1**, showing biased and unbiased direction of approach of ethyl radical. Energies are given in kcal/mol, with MN15 single-point values shown in parentheses.

sis shows similar π–π interaction regions in both **TS1** and **TS1′**, as indicated by the blue circles in Figure 4A. In **TS1**, weakly attractive interaction regions are observed between the ethyl group and both the phenyl substituent of the allene and a nearby ligand phenyl group, as indicated by the green circles. In contrast, the corresponding region between the ethyl group and the allene phenyl substituent in **TS1′** exhibits relatively greater repulsive character, as indicated by the orange circle. Although the NCI analysis is qualitative, these differences are consistent with the more favorable overall interfragment interaction in **TS1** identified by the D/I analysis and suggest that the energy difference may arise from the combined influence of multiple weak interactions and structural factors rather than from a single isolated contact.

To further explore the possible roles of the allene substituent and the attacking radical, their substituents were varied independently (Figure 4B). Replacing the phenyl substituent on the allene (R^1 = Ph) with a methyl group (R^1 = Me) decreases the free-energy difference between the competing transition states from 3.5 (5.3) kcal/mol for **TS1**/**TS1′** to 1.5 (2.2) kcal/mol for **TS3**/**TS3′**. Additional D/I analysis shows that the interfragment interaction-energy advantage nearly disappears, with ΔE_{int} changing from −2.9 (−4.0) to 0.1 (0.1) kcal/mol, while the remaining electronic-energy preference for **TS3** arises primarily from its lower distortion energy (Supporting Information File 1, section IV). Together with the NCI results, this change supports an important role of the allene aryl group in establishing the differential interaction between the approaching radical and the Fe–ligand–allene fragment. However, the effect of replacing Ph with Me cannot be attributed exclusively to π–π interactions. In contrast, replacing the attacking ethyl radical with a larger and more polarizable benzyl radical gives a free-energy difference of 3.7 (4.7) kcal/mol between **TS4** and **TS4′**, comparable to that obtained for the parent **TS1**/**TS1′** pair. The interfragment interaction continues to favor **TS4**, with ΔE_{int} = −1.7 (−2.7) kcal/mol, and is reinforced by a lower radical distortion energy (Supporting Information File 1, section IV). Together, these results support the contribution of differential interfragment interactions to the observed selectivity, while showing that their balance with distortion depends on the substituents.

Since the interactions around the reacting fragments are also influenced by the ligand structure, the role of the ligand in controlling the *Z*/*E*-selectivity was examined by calculating the competing C–C-bond-forming transition states with a flat, tridentate terpyridine *N,N,N*-pincer ligand, **L1** (Figure 4C). Using B3LYP-D3BJ, the pathway leading to the *Z*-alkene through **TS1_L1** is favored over the *E*-forming pathway through **TS1′_L1** by only 0.5 kcal/mol, corresponding to a predicted *Z*/*E*-ratio of approximately 2:1. Upon MN15 single-point correction, this small energetic preference is reversed, changing the predicted *Z*/*E*-ratio from 2:1 to 1:1.4. This functional dependence further indicates that the two pathways are effectively indistinguishable within the accuracy of the calculations. The optimized structures suggest that this diminished selectivity arises from the planar and relatively open coordination environment provided by **L1**. In both competing transition states, the coordinated allene can interact with the ligand π-system, while the terminal carbon remains similarly accessible to attack by the ethyl radical from either direction. Consequently, the flat tridentate **L1** ligand provides little differentiation between the two radical-approach trajectories, leading to nearly identical activation barriers (Figure 4D).

Following the formation of alkenyliron intermediate **IV**, the allylic radical undergoes the second C–C-bond-forming step through competing quartet and sextet pathways. Along the quartet pathway, the allylic radical coordinates to the iron center before undergoing inner-sphere reductive coupling through ^{4}**TS2** as indicated by the short Fe–C(allyl) distance of 2.22 Å (Figure 5). In contrast, the corresponding sextet transition state, ^{6}**TS2**, retains an outer-sphere character, with a substantially longer Fe–C(allyl) distance of 3.17 Å. These mechanistic assignments are consistent with the corresponding IRC calculations [34,35], which connect ^{4}**TS2** to an Fe-bound allylic radical intermediate and ^{6}**TS2** to an unbound radical pair. The activation barrier along the quartet pathway is lower than that along the sextet pathway by 6.0 kcal/mol at the B3LYP-D3BJ level and by 6.3 kcal/mol using MN15 single-point correction. Moreover, the activation barrier remains substantially lower than that of the preceding alkylferration step, confirming that the second C–C-bond formation is not rate-determining. Subsequent product dissociation furnishes the dialkylated alkene and generates a reduced iron species, which is regenerated to the active Fe(II) state through comproportionation with the Fe(III) precatalyst, thereby completing the catalytic cycle.

To examine alternative C–C-bond-forming pathways and their possible reactivity to give side-products, competing ethyl- and allylic radical additions were investigated (Figure 6). For the ethyl-radical addition to the iron-coordinated allene, **TS5** and **TS6**, corresponding to alternative addition sites, lie at 39.4 (37.5) and 34.0 (31.8) kcal/mol, respectively. Both are substantially higher in energy than **TS1** at 26.4 (25.1) kcal/mol, supporting the preference for the addition mode leading to the desired product. Fe-free addition of the allylic radical to phenylallene was also examined. **TS7**, **TS8**, and **TS9** lie at 24.7 (27.4), 19.2 (21.0), and 26.1 (29.1) kcal/mol, respectively. Both B3LYP-D3BJ and MN15 functionals favor addition through **TS8**. These additions generate carbon-centered radicals that

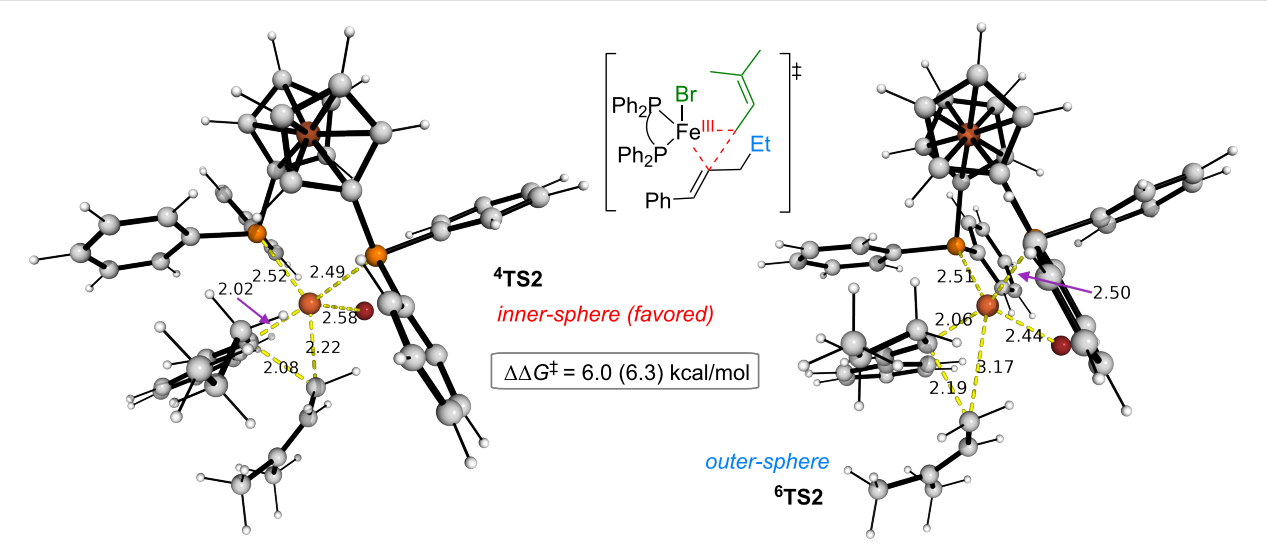

Figure 5: DFT-optimized structures for ^{4}**TS2** and ^{6}**TS2**.

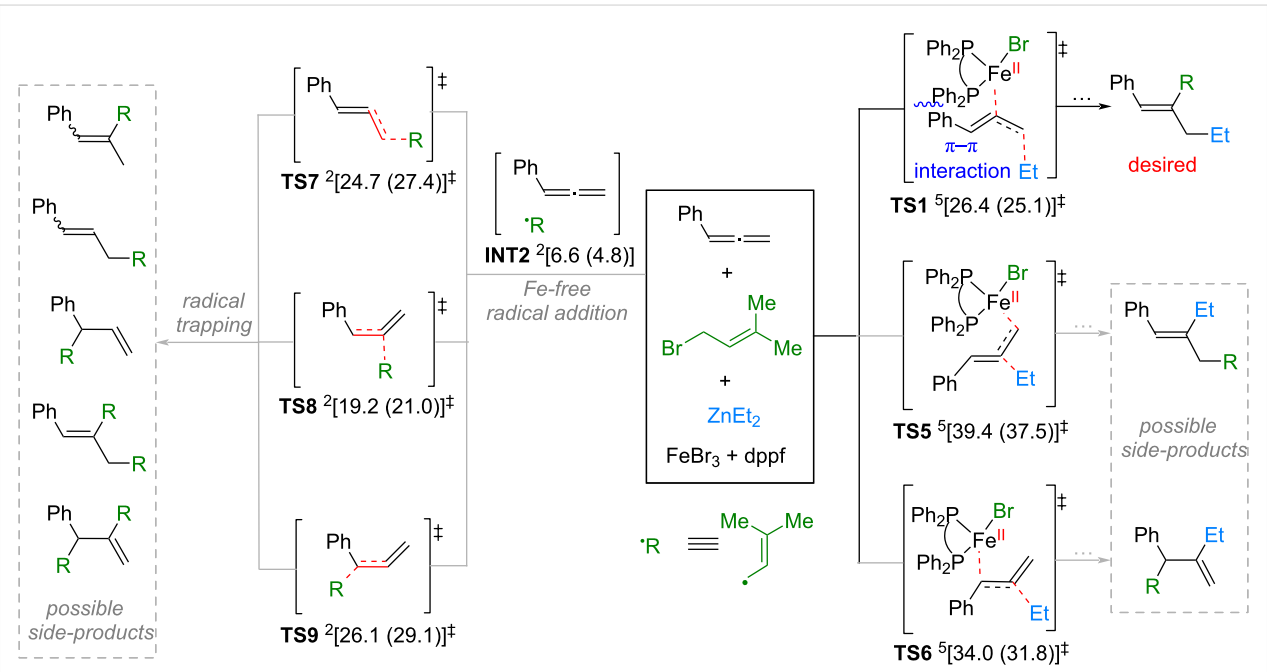

Figure 6: Investigation of possible side-product-formation pathways. Gibbs free energies are referenced to **I_quintet** for **TS1**, **TS5**, and **TS6**, and to the separated allylic radical and phenylallene for **INT2** and **TS7–TS9**. All energies are given in kcal/mol, with MN15 single-point values shown in parentheses. Superscripts in front of square brackets denote the spin states of the species.

could undergo subsequent trapping and product-forming steps, providing possible routes to the side-products shown in Figure 6.

Conclusion

In conclusion, our DFT calculations provide a unified mechanistic account of the iron-catalyzed three-component dialkylation of allenes. The revised thermochemical treatment and MN15 single-point calculations support the key mechanistic conclusions derived previously by Zhang and Koh [18]. The stereoselectivity is established during the initial outer-sphere addition of an ethyl radical to the iron-bound allene, whereas the competing inner-sphere migratory-insertion pathways are kinetically unfavorable and inconsistent with the experimentally observed selectivity. Distortion/interaction analysis shows that the preference for the *Z*-forming transition state originates

primarily from the more favorable interfragment interactions, which more than compensate for its greater structural distortion than in the *E*-forming transition state. Additional substituent comparisons and D/I analyses show that the balance between interfragment interaction and distortion depends on the identities of the allene substituent and the attacking radical. The subsequent allylic radical coupling is kinetically accessible and does not alter the stereochemical outcome established in the first C–C-bond-forming step. Calculations of alternative radical-addition pathways further support the preference for the productive sequence and provide possible initial C–C-bond-forming routes to the observed side-products. Together with the near-degeneracy of the *Z*- and *E*-alkene products, these results demonstrate that the observed *Z*-selectivity is governed by transition-state energetics under kinetic control. The markedly reduced selectivity calculated for ligand **L1** highlights the importance of the ligand environment in differentiating the competing radical-approach trajectories. More broadly, this study illustrates how the coordination environment of iron can regulate open-shell radical reactivity and stereochemical outcomes in allene difunctionalization.

Computational Methods

In this study, the optimization of all geometric structures and frequency calculations of stationary points were performed at the B3LYP [28] -D3BJ [29] /def2-SVP [36,37] level using the Gaussian 16, Revision B.01 program [38]. Minima and transition structures on the potential energy surface (PES) were confirmed using harmonic frequency analysis at the same level of theory, showing respectively zero and one imaginary frequency. Where necessary, intrinsic reaction coordinate (IRC) [34,35] calculations were carried out. Additionally, single point corrections were performed using B3LYP-D3BJ/def2-TZVP [36,37] and MN15 [30]/def2-TZVP. TPSSh [39]/def2-TZVP and M06-L [40] /def2-TZVP single-point calculations were performed for **I** and **TS1** to assess the functional dependence of their spin-state energetics (Supporting Information File 1, section II, Table S1). The effect of tetrahydrofuran (THF) solvent was accounted for using the SMD continuum solvent model [41]. Gibbs free energies were further evaluated at the reaction temperature of 333.15 K using the CHEMSMART toolkit [42], with natural abundance weighted mass and a quasi-rigid-rotor-harmonic-oscillator (quasi-RRHO) treatment of vibrational entropies and enthalpies [25,26], together with a correction for the standard state change from 1.0 atm to 1.0 M [43]. DFT optimized structures and spin density plots (isosurface value = 0.01 a.u.) are visualized using PyMOL software [44]. The NCI indices calculated with the NCIPLOT software [45] were visualized at a gradient isosurface value of s = 0.5 a.u. at the B3LYP-D3BJ/DGDZVP [46,47] level of theory. For species involving open-shell characteristics, including doublet, triplet, quartet, quintet, and sextet radicals, we performed above-mentioned DFT calculations using the unrestricted formalism of the Kohn–Sham theory (UKS-DFT). Unless otherwise stated, the final corrected Gibbs free energies SMD (THF)-B3LYP-D3BJ (MN15)/def2-TZVP//B3LYP-D3BJ/def2-SVP are used for discussion throughout. All Gibbs energy values in the text and figures are quoted in kcal/mol. The workflow management and data analysis were automated by the CHEMSMART toolkit [42].

Supporting Information

All the optimized structures have been deposited and uploaded to zenodo.org (https://doi.org/10.5281/zenodo.23879209). Automation toolkit codes for quantum chemical calculations as well as for thermochemistry analysis and figure plotting are freely available at https://github.com/xinglong-zhang/chemsmart.

Supporting Information File 1

Detailed computational methods, visualizations of the DFT-optimized structures, and absolute energies obtained from the Gaussian calculations.
[https://www.beilstein-journals.org/bjoc/content/supplementary/1860-5397-22-142-S1.pdf]

Funding

The authors acknowledge the computational resources at the Central Research Computing Cluster at the Chinese University of Hong Kong, partially funded by the Academic Equipment Fund (Project Number 3036253), for computations performed in this work. X. Z. acknowledges the support of the Vice Chancellor Early Career Professorship Scheme Research Startup Fund (Project Code 4933634) and Research Startup Matching Support (Project Code 5501779) from the Chinese University of Hong Kong (CUHK).

Author Contributions

Zihan Li: data curation; formal analysis; investigation; software; validation; visualization; writing – original draft. Yin-Hon Yeung: formal analysis; investigation; validation; visualization; writing – original draft. Xinglong Zhang: conceptualization; data curation; formal analysis; funding acquisition; investigation; methodology; project administration; resources; software; supervision; validation; visualization; writing – original draft; writing – review & editing.

ORCID® iDs

Zihan Li - https://orcid.org/0009-0006-8093-308X
Yin-Hon Yeung - https://orcid.org/0009-0002-2479-0492
Xinglong Zhang - https://orcid.org/0000-0003-1698-692X

Data Availability Statement

All the optimized structures have been deposited and uploaded to zenodo.org (DOI: https://doi.org/10.5281/zenodo.23879209). Automation toolkit codes for quantum chemical calculations as well as for thermochemistry analysis and figure plotting are freely available at https://github.com/xinglong-zhang/chemsmart.

References

1. Yu, S.; Ma, S. *Angew. Chem., Int. Ed.* **2012,** *51,* 3074–3112. doi:10.1002/anie.201101460
2. Soriano, E.; Fernández, I. *Chem. Soc. Rev.* **2014,** *43,* 3041–3105. doi:10.1039/c3cs60457h
3. Ma, S. *Acc. Chem. Res.* **2009,** *42,* 1679–1688. doi:10.1021/ar900153r
4. Blieck, R.; Taillefer, M.; Monnier, F. *Chem. Rev.* **2020,** *120,* 13545–13598. doi:10.1021/acs.chemrev.0c00803
5. Ma, S. *Acc. Chem. Res.* **2003,** *36,* 701–712. doi:10.1021/ar020133k
6. Deng, S.-M.; Zhao, Y.-X.; Wang, C. *Tetrahedron Chem* **2023,** *8,* 100049. doi:10.1016/j.tchem.2023.100049
7. Singh, J.; Sharma, A.; Sharma, A. *Org. Chem. Front.* **2021,** *8,* 5651–5667. doi:10.1039/d1qo00955a
8. Yi, R.; Li, Q.; Xie, L.-Y.; Wei, W.-T. *Chem. Commun.* **2025,** *61,* 6426–6438. doi:10.1039/d5cc00597c
9. Qiu, G.; Zhang, J.; Zhou, K.; Wu, J. *Tetrahedron* **2019,** *75,* 1578–1589. doi:10.1016/j.tet.2019.02.046
10. Liu, L.; Ward, R. M.; Schomaker, J. M. *Chem. Rev.* **2019,** *119,* 12422–12490. doi:10.1021/acs.chemrev.9b00312
11. Sun, X.; Liu, T.; Yang, Y.-T.; Gu, Y.-J.; Liu, Y.-W.; Ji, Y.-G.; Luo, K.; Zhu, J.; Wu, L. *Adv. Synth. Catal.* **2020,** *362,* 2701–2708. doi:10.1002/adsc.202000214
12. Wu, Z.; Yu, H. *Tetrahedron Lett.* **2022,** *100,* 153892. doi:10.1016/j.tetlet.2022.153892
13. Storozhenko, O. A.; Festa, A. A.; Zolotareva, V. A.; Rybakov, V. B.; Varlamov, A. V.; Voskressensky, L. G. *Org. Lett.* **2023,** *25,* 438–442. doi:10.1021/acs.orglett.2c04214
14. Siau, W.-Y.; Zhang, Y.; Zhao, Y. *Top. Curr. Chem.* **2012,** *327,* 33–58. doi:10.1007/128_2012_315
15. Kudo, E.; Sasaki, K.; Kawamata, S.; Yamamoto, K.; Murahashi, T. *Nat. Commun.* **2021,** *12,* 1473. doi:10.1038/s41467-021-21720-4
16. Kim, D.; Pillon, G.; DiPrimio, D. J.; Holland, P. L. *J. Am. Chem. Soc.* **2021,** *143,* 3070–3074. doi:10.1021/jacs.1c00856
17. Ge, L.; Sinnema, E. G.; Pérez, J. M.; Postolache, R.; Castiñeira Reis, M.; Harutyunyan, S. R. *Sci. Adv.* **2023,** *9,* eadf8742. doi:10.1126/sciadv.adf8742
18. Tan, T.-D.; Tee, K. Z.; Luo, X.; Qian, P.-C.; Zhang, X.; Koh, M. J. *Nat. Synth.* **2025,** *4,* 116–123. doi:10.1038/s44160-024-00658-7
19. Fürstner, A. *ACS Cent. Sci.* **2016,** *2,* 778–789. doi:10.1021/acscentsci.6b00272
20. Neidig, M. L.; Carpenter, S. H.; Curran, D. J.; DeMuth, J. C.; Fleischauer, V. E.; Iannuzzi, T. E.; Neate, P. G. N.; Sears, J. D.; Wolford, N. J. *Acc. Chem. Res.* **2019,** *52,* 140–150. doi:10.1021/acs.accounts.8b00519
21. Ye, F.; Zheng, S.; Luo, Y.; Qi, X.; Yuan, W. *ACS Catal.* **2024,** *14,* 8505–8517. doi:10.1021/acscatal.4c01312
22. Liu, Z.; Zhang, L.; Luo, S.; Qi, X. *Angew. Chem., Int. Ed.* **2025,** *64,* e202506268. doi:10.1002/anie.202506268
23. Yan, X.; Wang, S.; Liu, Z.; Luo, Y.; Wang, P.; Shi, W.; Qi, X.; Huang, Z.; Lei, A. *Sci. China: Chem.* **2022,** *65,* 762–770. doi:10.1007/s11426-021-1210-y
24. Daru, A.; Hu, X.; Harvey, J. N. *ACS Omega* **2020,** *5,* 1586–1594. doi:10.1021/acsomega.9b03578
25. Grimme, S. *Chem. – Eur. J.* **2012,** *18,* 9955–9964. doi:10.1002/chem.201200497
26. Li, Y.-P.; Gomes, J.; Mallikarjun Sharada, S.; Bell, A. T.; Head-Gordon, M. *J. Phys. Chem. C* **2015,** *119,* 1840–1850. doi:10.1021/jp509921r
27. Radoń, M.; Drabik, G.; Hodorowicz, M.; Szklarzewicz, J. *Chem. Sci.* **2024,** *15,* 20189–20204. doi:10.1039/d4sc05471g
28. Becke, A. D. *J. Chem. Phys.* **1993,** *98,* 5648–5652. doi:10.1063/1.464913
29. Grimme, S.; Antony, J.; Ehrlich, S.; Krieg, H. *J. Chem. Phys.* **2010,** *132,* 154104. doi:10.1063/1.3382344
30. Yu, H. S.; He, X.; Li, S. L.; Truhlar, D. G. *Chem. Sci.* **2016,** *7,* 5032–5051. doi:10.1039/c6sc00705h
31. Tan, T.-D.; Serviano, J. M. I.; Luo, X.; Qian, P.-C.; Holland, P. L.; Zhang, X.; Koh, M. J. *Nat. Catal.* **2024,** *7,* 321–329. doi:10.1038/s41929-024-01113-8
32. Ess, D. H.; Houk, K. N. *J. Am. Chem. Soc.* **2007,** *129,* 10646–10647. doi:10.1021/ja0734086
33. Bickelhaupt, F. M.; Houk, K. N. *Angew. Chem., Int. Ed.* **2017,** *56,* 10070–10086. doi:10.1002/anie.201701486
34. Fukui, K. *J. Phys. Chem.* **1970,** *74,* 4161–4163. doi:10.1021/j100717a029
35. Fukui, K. *Acc. Chem. Res.* **1981,** *14,* 363–368. doi:10.1021/ar00072a001
36. Weigend, F.; Ahlrichs, R. *Phys. Chem. Chem. Phys.* **2005,** *7,* 3297–3305. doi:10.1039/b508541a
37. Weigend, F. *Phys. Chem. Chem. Phys.* **2006,** *8,* 1057–1065. doi:10.1039/b515623h
38. *Gaussian 16,* Revision B.01; Gaussian, Inc.: Wallingford, CT, USA, 2016.
39. Tao, J.; Perdew, J. P.; Staroverov, V. N.; Scuseria, G. E. *Phys. Rev. Lett.* **2003,** *91,* 146401. doi:10.1103/physrevlett.91.146401
40. Zhao, Y.; Truhlar, D. G. *J. Chem. Phys.* **2006,** *125,* 194101. doi:10.1063/1.2370993
41. Marenich, A. V.; Cramer, C. J.; Truhlar, D. G. *J. Phys. Chem. B* **2009,** *113,* 6378–6396. doi:10.1021/jp810292n
42. Zhang, X.; Tan, H.; Liu, J.; Li, Z.; Wang, L.; Chen, B. W. J. *arXiv* **2025,** 2508.20042. doi:10.48550/arxiv.2508.20042
43. Bryantsev, V. S.; Diallo, M. S.; Goddard, W. A., III. *J. Phys. Chem. B* **2008,** *112,* 9709–9719. doi:10.1021/jp802665d
44. *The PyMOL Molecular Graphics System,* Version 1.8; Schrödinger, LLC: New York, NY, USA, 2015.
45. Contreras-García, J.; Johnson, E. R.; Keinan, S.; Chaudret, R.; Piquemal, J.-P.; Beratan, D. N.; Yang, W. *J. Chem. Theory Comput.* **2011,** *7,* 625–632. doi:10.1021/ct100641a
46. Sosa, C.; Andzelm, J.; Elkin, B. C.; Wimmer, E.; Dobbs, K. D.; Dixon, D. A. *J. Phys. Chem.* **1992,** *96,* 6630–6636. doi:10.1021/j100195a022
47. Godbout, N.; Salahub, D. R.; Andzelm, J.; Wimmer, E. *Can. J. Chem.* **1992,** *70,* 560–571. doi:10.1139/v92-079

License and Terms

This is an open access article licensed under the terms of the Beilstein-Institut Open Access License Agreement (https://www.beilstein-journals.org/bjoc/terms), which is identical to the Creative Commons Attribution 4.0 International License (https://creativecommons.org/licenses/by/4.0). The reuse of material under this license requires that the author(s), source and license are credited. Third-party material in this article could be subject to other licenses (typically indicated in the credit line), and in this case, users are required to obtain permission from the license holder to reuse the material.

The definitive version of this article is the electronic one which can be found at:
https://doi.org/10.3762/bjoc.22.142